PHYSICAL REVIEW A VOLUME 45, NUMBER 5 1 MARCH 1992

Dynamics of synchronously pumped mode-locked color-center lasers

W. Forysiak and J. V. Moloney

Department of Physics, Heriot-Watt University, Edinburgh EH14 4AS, Scotland

(Received 29 July 1991)

Numerical simulations of mode locking in synchronously pumped $\mathrm{Tl}^0(1)$ color-center lasers are presented. An asymmetric response with respect to cavity mismatch and the origin of large-scale fluctuations in spontaneous-emission noise are described. It is shown that quasistationary pulse trains may be obtained on cavity tuning without a degradation in pulse quality.

PACS number(s): 42.60.Fc, 42.60.Da, 02.70.+d, 42.25.Bs

I. INTRODUCTION

In lasers with sufficiently large gain cross sections, such as dye lasers and color-center lasers, synchronous pumping can be used to generate trains of mode-locked picosecond pulses [1,2]. The principle of this technique is the strong periodic modulation of the gain medium by the output from an actively mode-locked laser and its main requirement is that the period between pump pulses is equal, or close, to the round-trip time of the laser cavity. From a dynamical viewpoint, the principal difference between the color-center laser and its dye laser counterpart is that the relaxation time of the color-center medium (t_1) is long, as opposed to short, compared with the cavity round-trip time (t_{rt}). Thus the mode-locking characteristics of each system are significantly different [3] and, for instance, it is necessary to pump a color-center laser many times above threshold to achieve mode locking [2], whereas a dye laser mode locks more readily.

Until recently most of the theoretical work concerning mode locking by synchronous pumping has been related directly to dye lasers. An exception is the analysis of Yasa [3] which applies to the case $t_1 \gg t_{\mathrm{rt}}$. In addition, Kelly, New, and Wood [4] and Kurobiro *et al.* [5] have applied a powerful numerical technique developed by Catherall and New [6] to investigate the mode-locking characteristics of $\mathrm{KCl{:}Tl}^0(1)$ and $\mathrm{NaCl{:}(F_2{}^+)}_H$ color-center lasers, respectively. This technique defines a set of pulse shaping operations per cavity round-trip time. These operations, which represent gain, spectral filtering, and a temporal shift, are then applied to an initial pulse profile which evolves according to the operation parameters. The effect of spontaneous emission is simulated by the inclusion of an additive noise term. In general, however, most simulations adopting this technique are confined to a narrow local time window surrounding the pump pulse. In addition, phase effects such as gain dispersion and group-velocity dispersion, which can play an important role in the generation of ultrashort pulses [7], are usually neglected in these rate-equation treatments.

In this paper, we study the mode-locking dynamics of a $\mathrm{KCl{:}Tl}^0(1)$ color-center laser. We adopt an alternative approach based on the solution of a simple, traveling-wave model derived from the Maxwell equations for a two-level atomic system [8]. We do not restrict the model to the vicinity of the pump pulse, but simulate the laser equations over the entire cavity period. There are no direct assumptions about the longitudinal mode structure of the laser, the output of which evolves from spontaneous-emission noise and is subject to the boundary conditions imposed at the cavity mirrors. Furthermore, by retaining the polarization and population terms (non-rate-equation theory) we include the gain dispersion effects inherent to a two-level atomic transition. Although computationally intensive, the traveling-wave approach is well suited to the time domain description of multimode laser phenomena. In particular, it may yet provide one of the best methods to numerically simulate the recently developed coupled cavity systems, such as the soliton laser [9,10], which utilize nonlinear external cavities to improve the mode-locking performance of color-center lasers.

II. MODEL

A detailed derivation of the model we study is given elsewhere [8], and also briefly outlined in Appendix A to clarify the scaling used here. We consider a Fabry-Pérot cavity but ignore all higher-order Fourier terms representing the polarization and population gratings generated by the counterpropagating fields. Thus the truncated system of scaled Maxwell-Bloch equations is given by

$$\pm\frac{\partial E^{\pm}}{\partial z'}+\frac{\partial E^{\pm}}{\partial t'}=-P_0^{\pm}\ ,$$

$$\frac{\partial P_0^{\pm}}{\partial t'}=-\Gamma_2(P_0^{\pm}+E^{\pm}D_0]+S^{\pm}\ , \tag{1}$$

$$\frac{\partial D_0}{\partial t'}=-\Gamma_1[D_0-A(t)-\tfrac{1}{2}(E^{+*}P_0^{+}+E^{-*}P_0^{-}+\text{c.c.})]\ ,$$

where $E^{\pm}$ represent the slowly varying envelopes of the forward and backward-going electric fields, $P_0^{\pm}$ the zeroth-order polarization terms associated with these fields, and D_0 the population inversion between the two atomic levels. The longitudinal coordinate has been scaled to the length of the lasing medium (L) and the time to L divided by the phase velocity. Γ_1 and Γ_2 represent the phenomenological damping constants for

D_0 and $P_0^{\pm}$, respectively. The term $A(t)$ is a phenomenological pumping term which is time dependent and establishes the population inversion required for lasing. $S^{\pm}$ are phenomenological stochastic source terms which represent fluctuating contributions to $P_0^{\pm}$, independent of $E^{\pm}$, and simulate the effects of spontaneous emission. Equations (1) together with the boundary conditions,

$$\begin{aligned} E^{+}(z=z_{m1},t) &= -r_1 E^{-}(z=z_{m1},t) , \\ E^{-}(z=z_{m2},t) &= -r_2 E^{+}(z=z_{m2},t) , \end{aligned} \tag{2}$$

where z_{m1} and z_{m2} are the positions of the mirrors forming the Fabry-Pérot cavity, comprise our model system. We note that in the color-center laser under consideration, the length of the lasing medium is approximately 0.1% of the distance between mirrors. The propagation of radiation in those parts of the laser cavity where no lasing medium exists is described by Eqs. (1) with all material variables discarded.

A number of the simplifying assumptions made in arriving at this model system merit further comment. Firstly, for the sake of simplicity we have made the crudest possible truncation of higher-order Fourier terms, ignoring all above the zeroth order. Thus the short-range spatial variation of the atomic variables, which arises due to the counterpropagating fields in a Fabry-Pérot cavity, is not described at all by the truncated equations. In certain cases, it is possible to argue that higher-order terms may be ignored if, for instance, diffusion washes out the phase gratings [11]. However, this argument does not apply to color-center crystals in which the atomic sites are fixed within the crystal lattice. Exactly how many Fourier terms are required to accurately represent a given standing-wave dynamical phenomenon, such as the mode-locking process studied here, is an open question [12,13]. To consider the short-range spatial variations at the crudest possible level one could follow Fleck's lead and retain only those terms up to first order. However, for simplicity and to keep the computational burden within reason (the addition of each Fourier term adds three equations to the model system) we ignore the small-scale spatial effects completely.

A second simplifying assumption concerns the simulation of spontaneous-emission noise. This should be a multiplicative colored noise with a weight determined by factors such as the inversion lifetime and cavity geometry, and a Lorentz spectrum of frequency width equal to the laser linewidth [6,8,14]. Instead we choose to simulate the source terms $S^{\pm}$ as an additive contribution of fixed amplitude but random, uniformly distributed phase, such that

$$S^{\pm}(z_j,t_i) = A_s e^{i\phi^{\pm}(z_j,t_i)} , \tag{3}$$

where A_s is constant and $\phi^{\pm}(z_j,t_i)$ are uniform deviates on the interval $[0,2\pi]$. We note that the apparent deficiencies of this simple treatment may not be as severe as at first sight, for two reasons: firstly, it has been shown that variation of the magnitude of $S^{\pm}$ over several orders of magnitude has little effect on mode locking by synchronous pumping [6], and secondly, reducing Eqs. (1) to difference equations, as required for their numerical solution, defines a spontaneous-emission spectrum which is indeed Lorentzian [8].

Finally, an important simplification concerns the phenomenological pumping function $A(t)$. We presume that this modulation follows exactly the optical pulse of the pumping laser and is therefore a train of Gaussian, or $\mathrm{sech}^2(t)$ functions of the appropriate durations, which act homogeneously over the axial extent of the lasing medium. Because the optical transit time of the color-center crystal is short by comparison with the pump-pulse duration, the second of these assumptions may be acceptable. However, from a dynamical viewpoint, the first may be inadequate because the transfer of excited states from the upper pump level to the lasing transition may occur on a time scale of the order of, or longer than, the pump pulse. To take account of this latter effect one would need to either add a rate equation to drive the pumping function, or increase the level structure of the model, neither of which we undertake in this study.

Given the direct pumping function considered here, it is straightforward to show that the continuous pumping level required to raise the gain sufficiently to overcome the losses at the mirrors is given by

$$A > A_{\mathrm{con}} = \tfrac{1}{2}\ln\left[\frac{1}{r_1 r_2}\right] . \tag{4}$$

We are primarily interested in the generation of population inversion by trains of pump pulses of short duration compared with the inversion lifetime. In this case, good estimates of the lasing thresholds can be made by treating the pump pulses as δ functions and simply integrating over their areas. For a single Gaussian pulse,

$$A(t) = A_{\max} e^{-4\ln 2\, t^2/t_{\mathrm{FWHM}}^2} , \tag{5}$$

of full width at half maximum, t_{FWHM}, the amplitude required to reach lasing threshold is given by

$$(A_{\max})_{\mathrm{thr}} = \left[\frac{\ln 2}{\pi}\right]^{1/2} \ln\left[\frac{1}{r_1 r_2}\right] \frac{t_1}{t_{\mathrm{FWHM}}} , \tag{6}$$

where $t_1 \gg t_{\mathrm{FWHM}}$ so that $(A_{\max})_{\mathrm{thr}} \gg A_{\mathrm{con}}$, as expected. For trains of pulses separated by interval t_p, where $t_1 \gg t_p \gg t_{\mathrm{FWHM}}$, this amplitude is reduced by the factor

$$f_t = \frac{1}{1-e^{-t_p/t_1}} \approx \frac{t_1}{t_p} . \tag{7}$$

Therefore the threshold amplitude for a train of Gaussian pump pulses satisfying the above criteria and given approximately by

$$(A_{\max})_{\mathrm{thr}} \approx 2\left[\frac{\ln 2}{\pi}\right]^{1/2} \frac{t_p}{t_{\mathrm{FWHM}}} A_{\mathrm{con}} \tag{8}$$

is considerably higher than the cw pump threshold, but greatly reduced with respect to the single-pulse threshold. However, to achieve mode locking by synchronous pumping it is necessary to strongly modulate the gain [2,4] and therefore to pump the system at many times lasing threshold. It is convenient, therefore, to use the single-pulse threshold $(A_{\max})_{\text{thr}}$ defined in (6) as a measure of pumping strength, moreover, since it provides a clear picture of the depth of gain modulation produced by each pump pulse. For the KCl:Tl^0(1) color-center laser parameters given below in Table I ($t_1 = 1.6$ μs, $t_p = 10$ ns) a pumping strength of $1.0(A_{\max})_{\text{thr}}$ corresponds to 160× above lasing threshold. Thus, in order to significantly modulate the gain, by say tens of percent, it is necessary to pump tens of times above first lasing threshold. Experimentally, factors of approximately 10× are needed for acceptable mode locking [2], whereas the theoretical results using the pulse shaping operation approach [4] indicate a factor of around 100×. To determine accurately the mode-locking threshold using the approach presented here is computationally time consuming because the laser dynamics become increasingly slow near the threshold. Nevertheless, our few low pump power calculations indicate that the mode-locking threshold for system (1) lies below 16× lasing threshold, as described further below.

To consider mismatches between the round-trip time of the laser cavity (t_{rt}) and the pump period (t_p) we keep the laser cavity length fixed and vary t_p. In this way, mismatch times ($t_m = t_{\text{rt}} - t_p$) and variations of fractional values of Δt (the time step of our numerical scheme) can be simulated because a train of Gaussian functions of periodicity $t_p = (k + i/j)\Delta t$, where i, j, and k are integers, is easily generated on a numerical grid of time step Δt. In contrast, t_{rt} can be varied by only integer multiples of Δt, because the discretized cavity length comprises an integer number of spatial zones, each corresponding to a propagation time of Δt.

To enable wavelength tuning and to limit the spectral bandwidth most color-center laser cavities include a Fabry-Pérot étalon, which can be modeled as a spectral filtering element [4,5]. The spectral bandwidth of our model system is controlled solely by the linewidth of the laser transition. (We note that on a numerical grid of temporal spacing Δt, the spectral bandwidth is limited by the Nyquist frequency $1/2\Delta t$.) An additional filter could be readily introduced without a significant computational overhead because spectral filtering in the time domain can be performed by accurate and efficient algorithms [6,15]. However, since the gain bandwidth our model can consider is limited by the inverse of Δt to values comparable to that of a typical bandwidth limiting étalon, as discussed below, we have no need of an additional filter and instead utilize the entire bandwidth available.

TABLE I. Parameter values used for computations. t_2 is a compromise value; A_s is chosen arbitrarily (see body of text).

Parameter	
L_{cav}	1.5 m
L	1.5 mm
r_1	1.0
r_2	$\sqrt{0.8}$
N	3.0×10^{18} cm^{-3}
σ	2.0×10^{-17} cm^2
η	1.47
t_1	1.6 μs
t_2	2 ps
A_s	1.0×10^{-6}
t_p	≈ 10 ns
t_{FWHM}	80 ps

To solve our model system (see Appendix B), the partial differential equations (1) were reduced to finite difference form using a second-order scheme based on the method of characteristics, due to Fleck [8]. The five resulting implicit difference equations were then iterated using the explicit scheme suggested by Fleck and based on linearly extrapolating the inversion variables from two previous integration cycles. To check the validity of these results a second solution method using a Newton-like iteration loop to solve the implicit difference equations was also developed. Because this latter implicit scheme was computationally between five and ten times more expensive than the explicit method, it was used relatively sparingly, in which cases agreement between the two schemes was confirmed to be good.

The accurate reduction of Eqs. (1) to finite difference form requires the discretization time interval Δt to be smaller than the shortest time constant, which is t_2, the polarization relaxation time. Thus in all calculations described below an upper limit of approximately $t_2/4$ was set on Δt. Since the color-center bandwidth

$$\Delta\nu_b = \frac{1}{\pi t_2} \tag{9}$$

is extremely large (i.e., multi-THz) and the color-center medium is short (1–2 mm), with a transit time of a few ps, it is necessary to use very small values of Δt with respect to the cavity round-trip time. Therefore, in a typical calculation described below, each cavity round-trip corresponds to approximately 20 000 integration cycles. Furthermore, because the pulse dynamics evolve over hundreds of round-trips, many of our computations stretch to multimillion cycles and hence our previous concern with simplifying the Fabry-Pérot model.

III. NUMERICAL RESULTS

The Fabry-Pérot geometry we consider is shown in Fig. 1. The parameter values for a typical KCl:Tl^0(1) color center are given in Table I. The lasing medium is placed $\frac{1}{4}$ of the way from the output coupler and divides the cavity into three zones. Equations (1) describe the interaction within the central zone. Either side, the propagation of radiation in free space is managed by an array-pointer system which returns the outgoing electric fields to the medium, subject to reflection from one of the mirrors and the appropriate time delay. Unfortunately, because of computational power restrictions, it is not possible to solve the model for values of the dephasing time t_2, corresponding to the full multi-THz bandwidth of the color-center medium. The value of t_2 suggested by the color-center bandwidth of 650 cm^{-1} is of the order of 15 fs, which is clearly impractical for our numerical scheme. However, since this enormous bandwidth is usually limited, in both experimental and model systems, by filters of

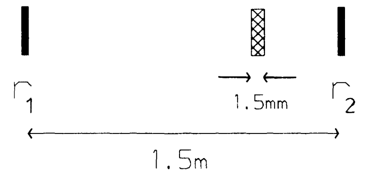

FIG. 1. Schematic diagram of the color-center laser cavity under consideration. The cavity is 1.5 m long and the 1.5-mm color-center medium is placed $\frac{1}{4}$ of the way from the output coupler. The left-hand mirror is perfectly reflecting and the output coupler has an intensity reflection coefficient of 0.8. The forward ($+ve$) direction is defined from left to right.

≈1 THz bandwidth (filter times of between 0.8 and 0.1 ps were used in [4,5]), we can increase t_2 to consider a similarly bandwidth-limited system, but with this limitation imposed solely by the lasing transition. Therefore, in the calculations described here, we choose $t_2=2$ ps and aim for a good qualitative representation of the mode-locking process. Since the axial mode spacing of a 1.5-m Fabry-Pérot geometry is 100 MHz and $t_2=2$ ps corresponds to a gain bandwidth of approximately 160 GHz, we are nonetheless considering in excess of 1500 longitudinal modes under the gain line.

We divide the 1.5-mm-long lasing medium into (n_z-1) spatial zones defined by n_z points and the empty regions to the left and right into n_l and n_r zones, represented by n_l and n_r points, respectively. This corresponds to an integration time of $\Delta t=(\eta L/c)/(n_z-1)$ and an optical round-trip time of $t_{\mathrm{rt}}=2(n_z+n_l+n_r-1)\Delta t$. Given $t_2=2$ ps, we choose $n_z=15$ for the majority of our calculations, so that $\Delta t=0.525$ ps. With the empty regions defined by $n_l=7136$ and $n_r=2378$, the optical round-trip time is 10.0044 ns, requiring a total of 19 056 iterations.

The early part of the evolution of the mode-locked laser pulse from noise is shown in Figs. 2(a)–2(f). In these and all subsequent figures, the intracavity forward-going field intensity at the right-hand boundary of the lasing medium is plotted as a function of local time t_{loc}, defined to be zero at the peak of the pumping function. This representation provides a clearer picture of the relative timings of events within the lasing medium than the laser output, which can be easily inferred since it is simply proportional to the displayed quantity and delayed by the transit time from the medium to the output coupler. Superimposed on these intensity profiles are the corresponding variations of the inversion variable, D_0, measured at the same point in the lasing medium. Scaled units are used in all figures. We recall that one scaled time unit corresponds to the medium transit time of 7.35 ps and that therefore one cavity round-trip corresponds to approximately 1361 local time units. Thus each individual picture of Fig. 2 represents the pulse evolution over

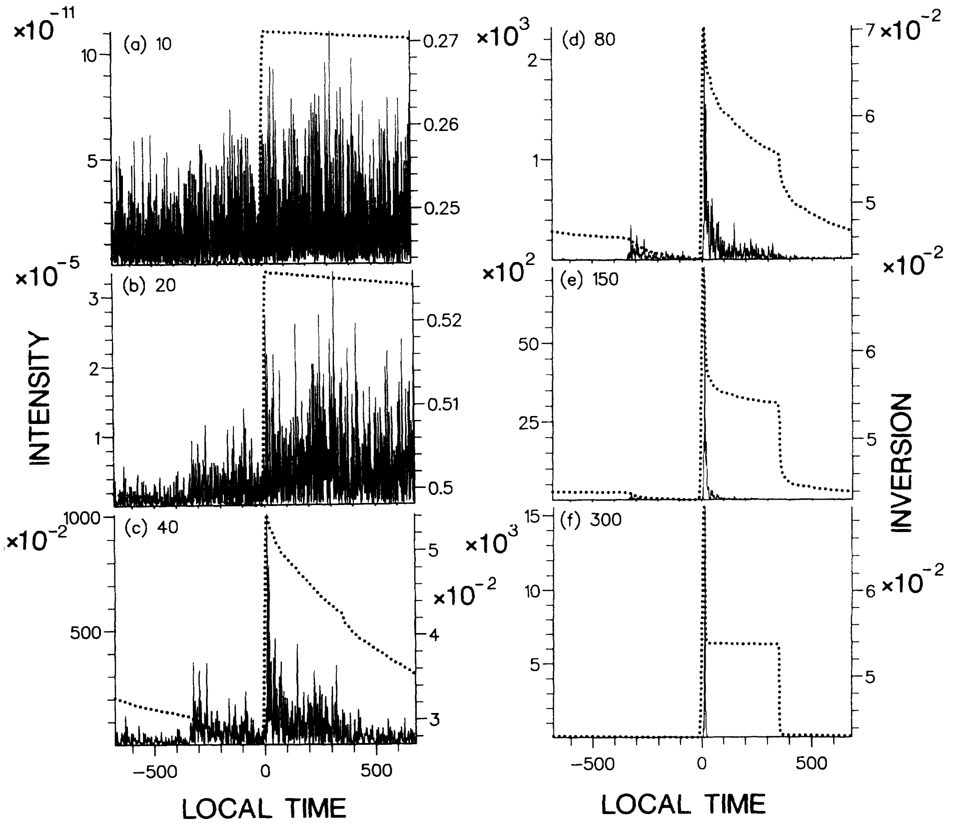

FIG. 2. Early evolution of the mode-locked pulse train. The forward-going field intensity $[|E^+(n_z)|^2]$ and inversion $[D_0(n_z)]$ at the right-hand boundary of the medium are plotted as functions of the local time over one round-trip period after (a) 10, (b) 20, (c) 40, (d) 80, (e) 150, and (f) 300 round-trips. Note the change of scales in each figure.

a single cavity round-trip, with the pump pulse centered on zero local time. The intracavity intensity in these and all subsequent figures is measured in units of 2.05 kW/cm^2 (see Appendix A), $\frac{1}{5}$ of which is transmitted through the output coupler.

For the computation depicted in Fig. 2 the pump-pulse amplitude was chosen to be $0.5(A_{\max})_{\text{thr}}$ (80× lasing threshold) and its periodicity (or transit time) t_p to exactly equal the round-trip time t_{rt}. The spontaneous-emission amplitude was chosen quite arbitrarily to be $A_s = 10^{-6}$, in the knowledge that the resulting noise intensity (of order A_s^2) would be much smaller than pulsed intensity (at least of order 1). In each of Figs. 2(a)–2(f) the pump induced modulation of the gain is reflected in the rapid rise of the inversion at zero local time. Because of the strong pumping, the inversion is raised rapidly above threshold while initially the fields remain small, as shown in Fig. 2(a). At this stage, the field intensity is beginning to rise above the spontaneous-emission noise level but its form is still that of amplified noise. From this point on [Figs. 2(b) and 2(c)] the fields undergo rapid nonlinear amplification which ultimately has two effects. Firstly, the fields grow large enough to begin to deplete the inversion significantly and it is swiftly reduced to the near-threshold region. This rapid reduction and the associated giant pulse envelope is reminiscent of Q switching and occurs because the relatively long t_1 allows the inversion to build up more rapidly than the fields. We note that at its peak, the inversion is approximately 12 times above lasing threshold. However, since the lasing threshold is given by $D_0 \approx 0.0558$, which corresponds to only 1.24% of the active atom density, it is not an unphysically large figure. Secondly, a pulse selection process takes place, evidence of which is apparent after 20 round-trips [Fig. 2(b)] and obvious after 40 [Fig. 2(c)]. As this proceeds, the field intensity, which is initially aperiodic, begins to develop similarities from round-trip to round-trip.

The latter stages of the mode-locked pulse selection process are shown after 80, 150, and 300 round-trips in Figs. 2(d)–2(f), where the gradual temporal smoothing of the cavity fields as a result of their amplification is evident. It is clear that those sections of the cavity fields, both forward and backward, which are about to enter the lasing medium as the pumping pulse acts on it, receive preferential gain because they are subject to amplification by the maximum inversion in any given round-trip. In Fig. 2 these preferred forward-going features are those at $t_{\text{loc}} = 0$, while the associated backward-going features show up in the forward field at $t_{\text{loc}} \approx -t_{\text{rt}}/4$ because the fields are folded back on themselves at the mirror boundaries (propagation from the medium to the output coupler and back takes time $t_{\text{rt}}/4$). Figures 2(d)–2(f) show the forward-going features being enhanced at the expense of the backward, so that ultimately the mode-locked pulse forms at the tail of the pumping pulse. A simple explanation for this effect is that although both forward and backward features undergo a simultaneous first amplification during any one round-trip period, the forward feature returns to the medium (now traveling in the backward direction) before the backward (then traveling in the forward direction), and is therefore subject to a preferential second amplification. We note that once the mode-locked pulse is formed, as in Fig. 2(f), the cavity acts essentially unidirectionally with the pulse moving to and fro through the amplifying medium. Thus the second rapid downward gradient of Fig. 2(f) corresponds to the amplification of the pulse as it moves in the backward direction.

The detailed pulse evolution within a narrow local time window in the vicinity of the pump pulse is shown in Fig. 3. The mode-locked pulse does not evolve as a single maximum as suggested by Figs. 2, but rather the maxima which emerge at the tail of the pump pulse are delayed slowly with respect to it (i.e., they propagate to the right in the local time frame), reach maximum amplitudes themselves, and then decay, giving way to other maxima ahead of them. This rightward motion reflects the group-velocity-induced time delay of the propagating mode-locked pulse with respect to the pump pulse whose periodicity is fixed by $t_p = t_{\text{rt}}$ to the round-trip time of undispersed light within the cavity. Thus there is an *effective mismatch* between t_p and the round-trip time of the mode-locked pulse, which arises from the finite polarization response time of the color-center medium. In essence this is analogous to the effective mismatch discussed by Catherall and New [6] which in their case arises from the group time delay imposed by a spectral filtering operation. However, whereas in their case it is possible to select zero effective mismatch by choosing appropriate values of t_p and the filter response time, the effective mismatch in our case is unknown *a priori* because the group-velocity time delay depends on the actual form of the mode-locked pulse.

After 500 (pump-pulse) transits the mode-locked pulse

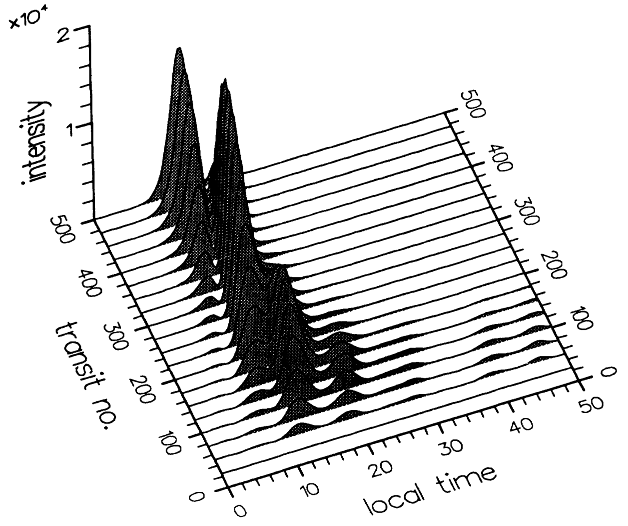

FIG. 3. Pulse profile evolutions $[|E^+(nz)^2|]$ over the first 500 transits displayed at 25 transit intervals. The pump pulse, which is centered at $t_{\text{loc}} = 0$, is approximately 11 local time units wide (FWHM). Because $t_p = t_{\text{rt}}$ the pump-pulse transit number also corresponds to the cavity round-trip number, which is not true generally.

consists of a main maximum of width 21 ps (FWHM) with a small trailing satellite and is situated at the tail of the pump pulse (see Fig. 4). Beyond this point the pulse evolution changes as shown in Fig. 5. After the main pulse grows and its trailing satellite diminishes, it no longer decays in favor of another leading satellite, but remains a robust single maximum and is gradually delayed with respect to the pump pulse. Over the following 3000 transits the pulse remains single humped, with a slowly varying height and width. Figure 6 summarizes the evolution of the pulse peak intensity and position as a function of transit number. The slight reduction in intensity after approximately 2000 transits is associated with a *perturbative event* (these are discussed in detail below). However, the rightward traversal rate is almost constant throughout this phase and corresponds to a delay of approximately $\frac{1}{10}$ ps per round-trip. The final phase of the pulse evolution ensues when this traversal is complete after approximately 3500 transits as shown at the top of Fig. 5 and in Fig. 6. Beyond this point, the pulse suffers a loss in intensity, broadens slightly, and oscillates aperiodically in a position delayed approximately 380 ps from the pump pulse.

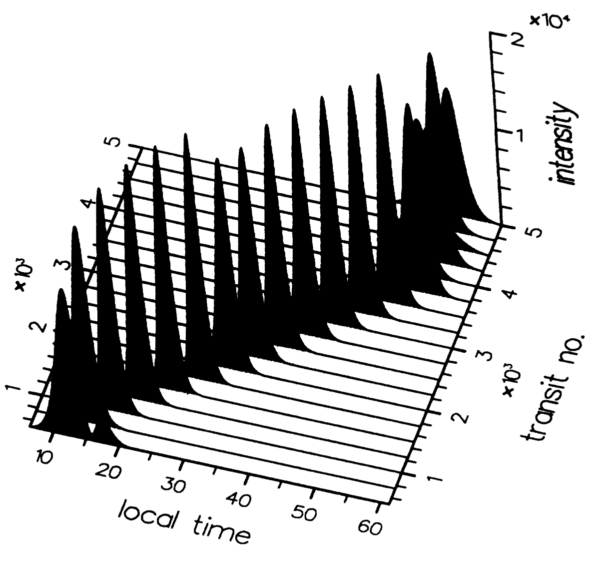

FIG. 5. Pulse profile evolutions from 500 to 5000 transits at 250 transit intervals. The intermediate translational movement corresponds to a delay of approximately $\frac{1}{10}$ ps per transit.

The detailed behavior of the pulse in its final evolution stage is shown in Fig. 7 (its position with respect to the pump is illustrated in Fig. 4). Exactly why the pulse chooses this particular delay is difficult to explain. However, it is clear that this delay must balance two opposing influences, on the one hand, the polarization-induced group time delay driving the pulse to the right, and on the other, the preferential gain experienced by the leading edge of the pulse, which arises since there is significant gain depletion by each amplifying pass, and tends to move the pulse to the left. By repeating our simulations with different *seeds* for the random number generator, we verified that although the ultimate pulse dynamics are a sensitive function of the seed, its mean position in local time is unchanged. Moreover, the transient behavior is similar in all cases, with the initial pulse buildup in the vicinity of the pump pulse, followed by a translation, and then some form of oscillation, or jitter. To verify that this jitter is sustained, the first computation was continued to over 20 000 transits during which time it showed no signs of attenuation. The mechanism of these sustained perturbations is certainly driven by the spontaneous-emission terms. In a further computation, the addition of these terms was inhibited after 6300 transits (i.e., well into the final phase) which resulted in a decay of the oscillation and a return to translational behavior. The subsequent reintroduction of the noise returned the oscillation to its original temporal position but with a different form to the original.

Given the association of these fluctuations in the pulse shape with the spontaneous-emission noise, it is possible to apply the same argument as Catherall and New [6] to explain their origin in the different velocities of the pulse envelope and the background noise of nonzero effective

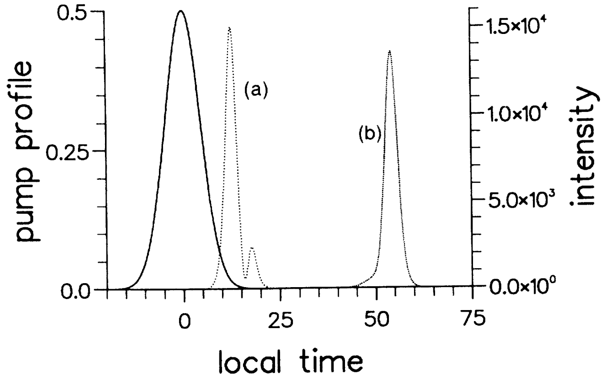

FIG. 4. Position of mode-locked pulse relative to pump pulse after (a) 500 and (b) 6300 transits.

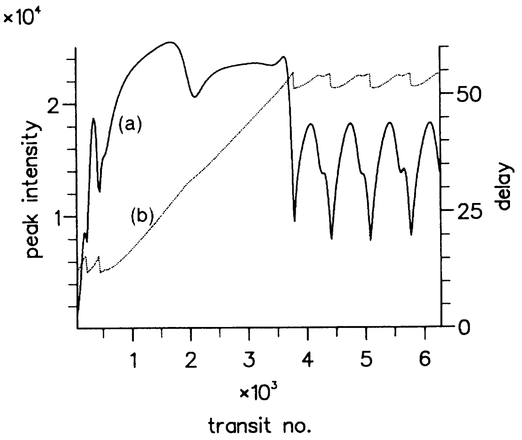

FIG. 6. Variation of (a) the maximum pulse intensity and (b) its delay with respect to the pump pulse vs pump-pulse transit number. The simultaneous discontinuities in both functions correspond to positions in which one maximum of the pulse exceeds another.

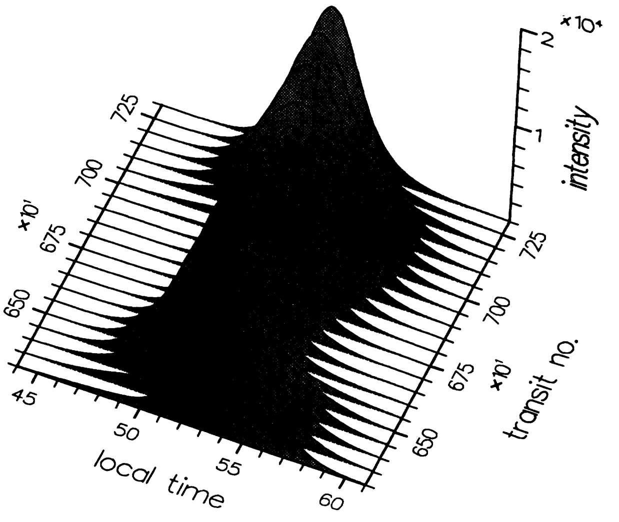

FIG. 7. Pulse profile evolutions in the final phase, displayed from 6300 to 7300 transits at 50 transit intervals.

mismatch. Thus these large-scale fluctuations arise from the amplitude and phase variations in the background noise which are amplified during translation through the pulse. Moreover, the second suggestion of Catherall and New [6], that it may be possible to correlate fluctuations in these systems with *phase waves* of the kind discussed in the context of swept gain amplifiers by Hopf and Overman [16], does seem to be valid here. Figure 8 shows the intensity and phase profiles along the pulse during three round-trips during the *perturbative event* at the front of Fig. 7. With each round-trip the phase curve moves slowly backward in local time, sweeping through the pulse as it does so. The perturbation, which rapidly accelerates the pulse to shift it forward in local time, is clearly correlated with the passage of the positive gradient portions of the phase. This itself is a signature of the electric field and polarization phases acquiring a significant nonzero phase angle [16]. During the remainder of the cycle the pulse is delayed relatively slowly until the process repeats again with the next reversal of the phase gradient. In common with the fluctuations described by Hopf and Overman, which are identical upon variation of the initial polarization by a factor of 100, these fluctuations appear relatively insensitive to the amplitude of the spontaneous-emission noise, which is, of course, applied continuously in this case. However, unlike the fluctuations described in [16] which vary pulse power and energy, those described here are fluctuations of power only. Although the peak power and pulse width vary by up to 60% in Fig. 6, the pulse energy remains constant to better than 0.01%.

To investigate the effect of mismatch we first increased the period of the pump laser in an attempt to match the polarization-induced group-velocity time delay and thereby eliminate the above-described jitter. The rate of translation of $\frac{1}{10}$ ps in Fig. 5 provided a guide for trial mismatch values and evolutions corresponding to mismatches (defined as $t_m = t_{\mathrm{rt}} - t_p$) of $-\Delta t/2$, $-\Delta t/3$, $-\Delta t/4$, $-\Delta t/5$, $-\Delta t/6$, $-\Delta t/8$, and $-\Delta t/10$ were studied. The best results from this set were obtained for $t_m = -\Delta t/4$, for which Fig. 9 describes the evolution of the pulse peak intensity and delay. Both parameters are seen to be varying very slowly during the latter stages of this figure, indicating a near-stable pulse approaching an equilibrium position. The pulse evolutions of Fig. 10 confirm this supposition. These near-optimum, quasistationary (strictly speaking, solutions to stochastic differential equations cannot be stationary) pulses have peak intensities of 51 MW/cm^2, widths of 16 ps, and are positioned at the tails of the pump pulses. Recalling that $\frac{1}{5}$ of the intracavity intensity is output coupled and presuming a spot size of $\omega_0 = 20$ μm at the crystal, the integrated pulse areas give output pulse energies of approximately 2.2 nJ per pulse. There appear to be no noise-mediated perturbations in this case, presumably because the relative velocities of the mode-locked pulse and the background noise are equal. Furthermore, there is almost negligible variation of the phase of the electric field along the pulse, as shown in Fig. 11. The pulse intensity in this figure is plotted on a natural logarithm scale to emphasize its smooth nature and to show there are no perturbations in its wings. The linearity of the wings indicates that it can be well fitted to a $\mathrm{sech}^2(t/t_w)$ shape with different t_w describing the rising and falling edges, since these clearly have different slopes. It compares

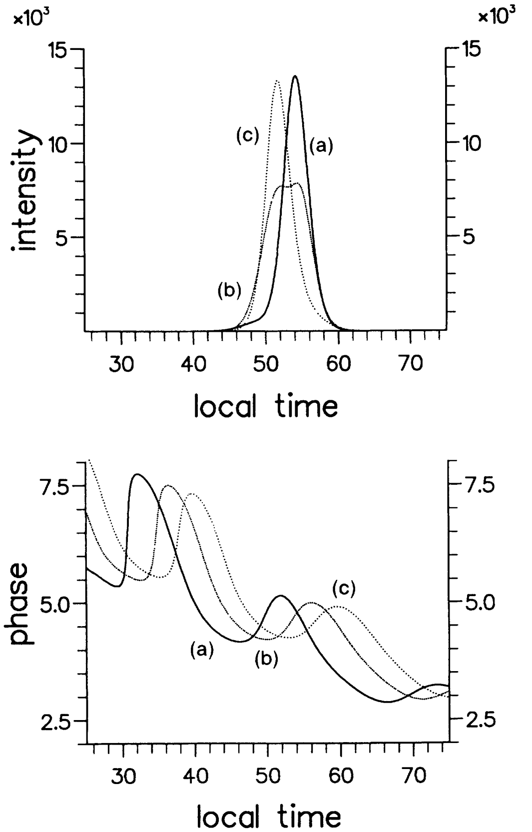

FIG. 8. Pulse profile evolutions together with variations of the field phase after (a) 6300, (b) 6440, and (c) 6550 transits. The phase wave moves slowly through the pulse profile, whose distortion and acceleration are correlated with the passage of the positive gradient of the phase.

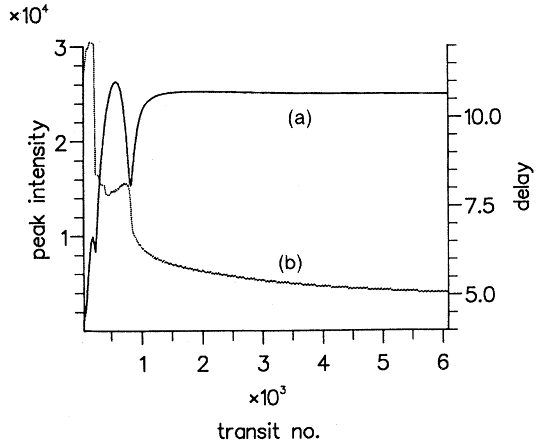

FIG. 9. Variation of (a) the maximum pulse intensity and (b) its delay with respect to the pump-pulse peak vs transit number for $t_m = -\Delta t/4$.

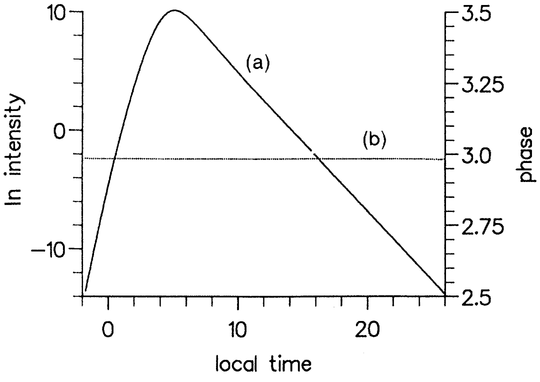

FIG. 11. Natural logarithm of the mode-locked pulse intensity (a) and the phase (b) of its electric field for $t_m = -\Delta t/4$ after 5800 transits.

with an equivalent shown in Fig. 12 obtained for $t_m = 0$, for which the perturbations associated with the phase wave are also evident in the wings of the intensity profile. We note, incidentally, that the strength of each phase wave is severely diminished by its interaction with the pulse maximum.

The remaining mismatch computations listed above divide into two behavioral categories, showing pulse evolutions similar to one of the two cases already described. For the two values of t_m less than optimum, the ultimate laser output is also a train of quasistationary pulses, examples of which are shown in Fig. 13. These pulses occur ahead of the optimum pulse and are consequently diminished and broadened (but of the same total energy). Whereas for $t_m = -\Delta t/3$, the pulse shows a significant tail indicating the possibility of satellite formation, this does not occur on decreasing t_m to $-\Delta t/2$, for which the resulting pulse is considerably broadened and follows the pump profile almost exactly. The peak intensities and pulse widths of these steady-state pulses, whose tuning range of $-\Delta t/2 < t_m < -\Delta t/4$ corresponds to a cavity length variation of ≈ 20 μm, are shown alongside comparable measures for mismatch values greater than optimum in Fig. 14. For these latter cases, the pulse evolutions are similar to those of zero mismatch, i.e., a transient involving a shift with respect to $t_{\mathrm{loc}} = 0$ followed by an oscillation. Thus the points for $t_m > -\Delta t/4$ in Fig. 14 are not absolute values, but correspond to averages over many thousands of transits. Figure 14 shows that the asymmetry in behavior extends beyond a division between stationary and nonstationary pulses, to the average parameters describing these pulses, which show a slower decrease in peak power and lesser broadening on tuning to t_m greater than optimum. The variation in average pulse position, for those cases resulting in nonstationary pulsation, is shown in Fig. 15. We note the addition of a number of points for positive values of t_m, which show the same qualitative behavior, but with a more rapid rightward translation and a diminished, broader, and more swiftly varying final oscillation (the sweep rate of

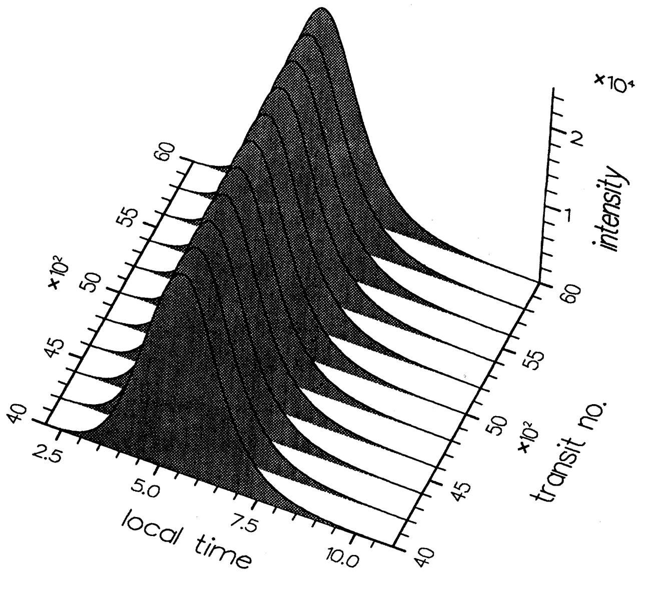

FIG. 10. Pulse profile evolutions displayed from 4000 to 6000 transits at 200 transit intervals for $t_m = -\Delta t/4$.

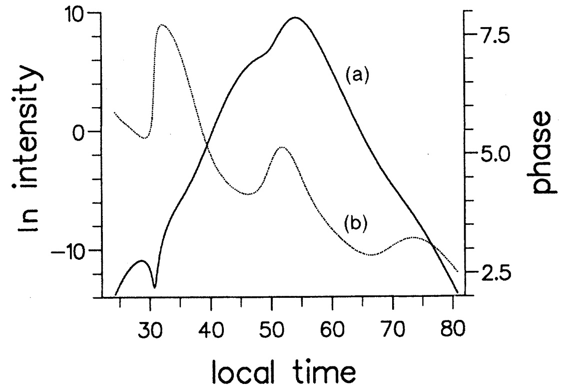

FIG. 12. Natural logarithm of the mode-locked pulse intensity (a) and the phase (b) of its electric field for $t_m = 0$ after 6300 transits, i.e., corresponding to Fig. 8(a).

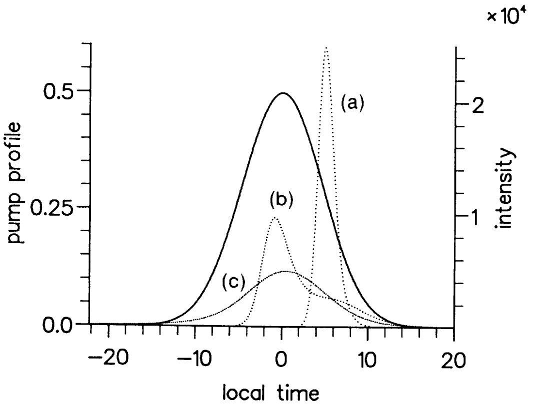

FIG. 13. Positions of the quasistationary mode-locked pulses relative to the pump pulse for (a) $t_m=-\Delta t/4$, (b) $t_m=-\Delta t/3$, and (c) $t_m=-\Delta t/2$.

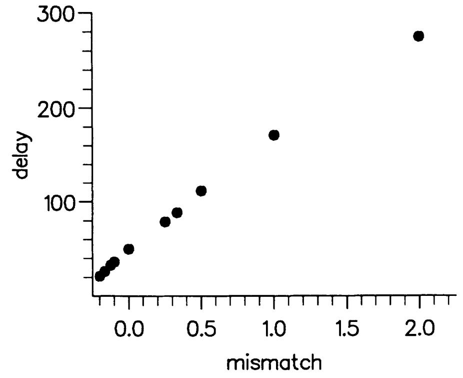

FIG. 15. Variation of the average peak pulse delay with mismatch, t_m.

the noise-induced perturbations through the pulse increases with t_m). Thus the same type of response extends over a range of approximately $-\Delta t/5<t_m<2\Delta t$, within which the mode-locked pulse can be far removed from the pump pulse, and delayed by as much as 2 ns when $t_m=2\Delta t$.

In the above discussion, t_m has been measured in units of Δt, because for our calculations the mismatch is most conveniently generated in fractional values of the discretization interval. However, in terms of the laser system under study, Δt is meaningless of course, and the relevant physical quantity is the polarization decay time t_2 ($\approx 4\Delta t$). To verify that this is indeed the case, we repeated a number of calculations with $n_z=22$, i.e., $\Delta t \rightarrow 2/3\Delta t$. These showed a rightward traversal and subsequent oscillation for $t_m>-t_2/18$, in agreement with Fig. 14 above. In addition, equivalent calculations to those generating quasistationary solutions in Fig. 14 gave stable pulses with the same characteristics (to better than 5%).

Thus far, we have described two regions of mode-locking behavior on variation of cavity mismatch: a relatively narrow region of quasistationary pulses bounded at high t_m by the optimum pulse shape, and a wider region of nonstationary pulses for t_m greater than optimum. Strictly speaking only the stationary pulses of the narrower region can be described as truly mode locked, but nevertheless, many of those nearby within the wider region are also well localized in time and space, and may be of greater peak intensity and shorter (on average) than some stationary ones. For instance, all the nonstationary pulses described in Fig. 14 are shorter than the stationary pulse for $t_m=-\Delta t/2$. In addition, they are predominantly single peaked. However, as t_m is increased within the wider region, mode locking gradually breaks down. Figure 16 shows the final stage of pulse evolution for $t_m=2\Delta t$. Although still apparently localized in time, the pulse form now consists of multiple maxima, evolving relatively quickly as the noise-induced perturbations are swept backward in local time through it. In addition, the logarithmic plot of Fig. 17(a) shows that a substantial fraction of the cavity field is above the spontaneous-emission noise level, as compared to the optimally mode-

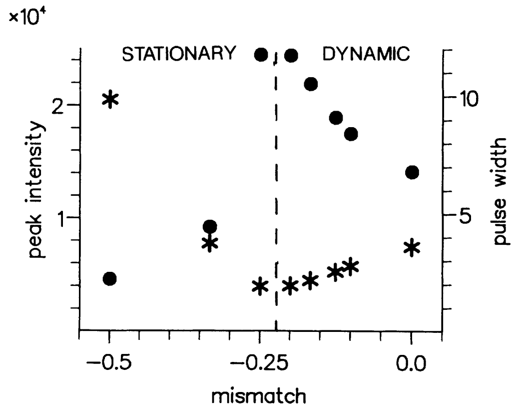

FIG. 14. Variation of average peak pulse intensities (●) and pulse widths (✱) with mismatch, t_m. The three leftmost points correspond to stationary pulses. The remaining nonstationary pulses are obtained from averages over thousands of transit periods, during the final pulse evolution stage.

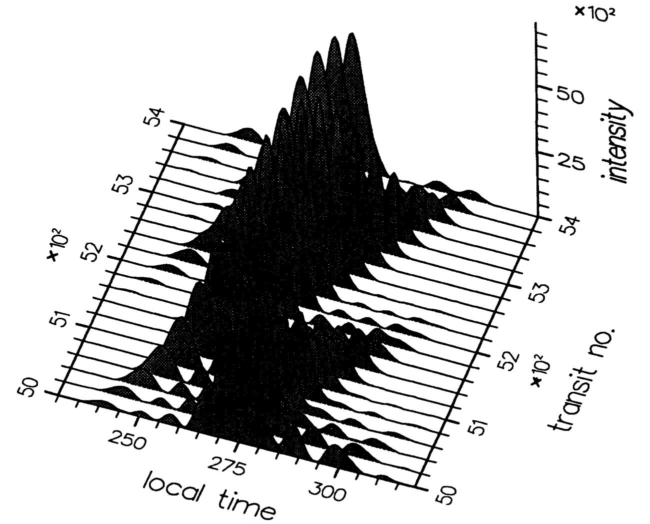

FIG. 16. Pulse profile evolutions displayed from 5000 to 5400 transits at 20 transit intervals for $t_m=2\Delta t$.

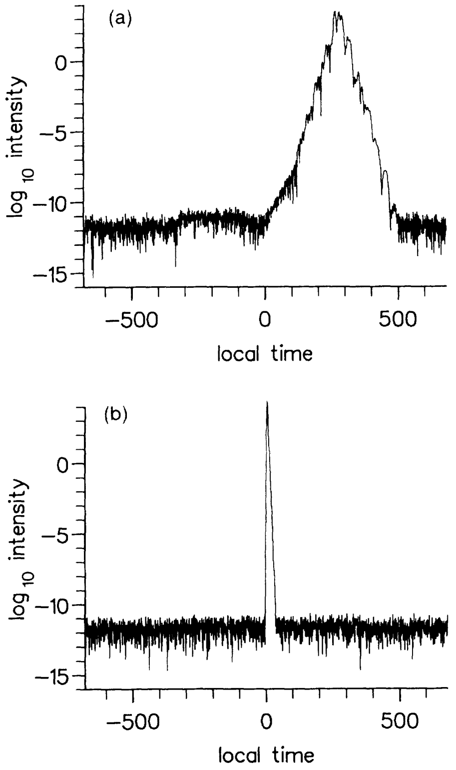

FIG. 17. Log$_{10}$ of the pulse forms during the final evolution phases over a single round-trip for (a) $t_m = 2\Delta t$, (b) $t_m = -\Delta t/4$.

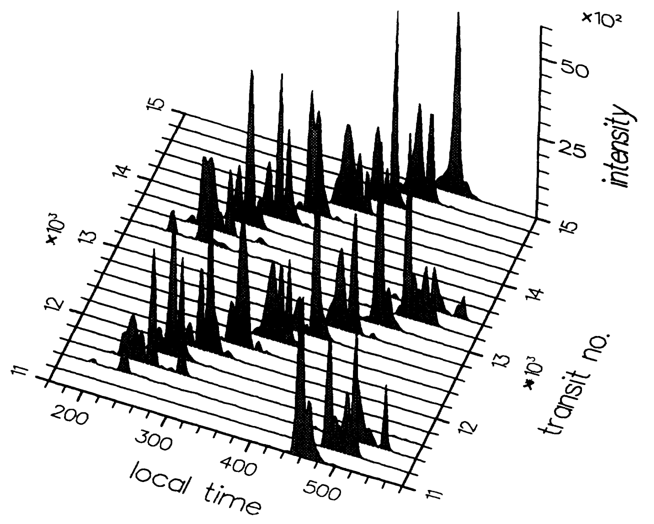

FIG. 18. Pulse profile evolutions displayed from 11 000 to 15 000 transits at 200 transit intervals for $t_m = 4\Delta t$.

locked case [Fig. 17(b)] for which the coherent part of the cavity field comprises but a few percent. With still further increase in t_m, the pulse form loses its positional stability in local time and begins to zigzag about a position corresponding to $t_{\text{loc}} \approx t_p/4$ as shown in Fig. 18. Thus the loss of mode locking to positive mismatch may be regarded as a gradual process in which the ever increasing sweep rate of the perturbations through the pulse structure causes increasing disruptions eventually leading to complete breakdown.

In contrast, as t_m is decreased from optimum, the breakdown in mode locking occurs via a different mechanism. Firstly, as the stationary pulse broadens, there is a rapid broadening of the coherent background, so that for $t_m = -\Delta t/2$ the background noise occupies barely half of the intracavity field. Then, as t_m is further decreased the pulse loses stability and begins to switch between two temporal positions, $t_{\text{loc}} = 0$ and $-t_p/4$, as shown in Fig. 19 for $t_m = -\Delta t$. As described earlier in Fig. 2, the latter position corresponds to the amplification of a pulse traveling in the backward, rather than forward direction, on arrival of the pump pulse. The frequency and form of the switches is random, and although the greatest pulses still occur in the vicinity of $t_{\text{loc}} = 0$, a large fraction of the pulse energy is periodically switched to the earlier occurrence time. In the laser output, this action manifests itself as an interruption of a train of single pulses per cavity round-trip, with a train of double pulses per round-trip, separated by $\frac{1}{4}$ of the round-trip time.

The origin of the switching behavior is the forward drift (right to left in Fig. 19) of both the main pulse structure and the perturbations caused by the negative mismatch. As for positive mismatch, this dictates the continual reshaping of the pulse structure, though it now occurs in the opposite direction. However, more importantly, in the vicinity of $t_{\text{loc}} = 0$, the leading edge must be diminished as it drifts forward of the pump pulse to positions where it experiences negative gain. It is as this process occurs that the simultaneous backward-going field may experience preferential gain and briefly overcome the forward-going field to yield the switching action. With further decrease in negative mismatch, the switch-

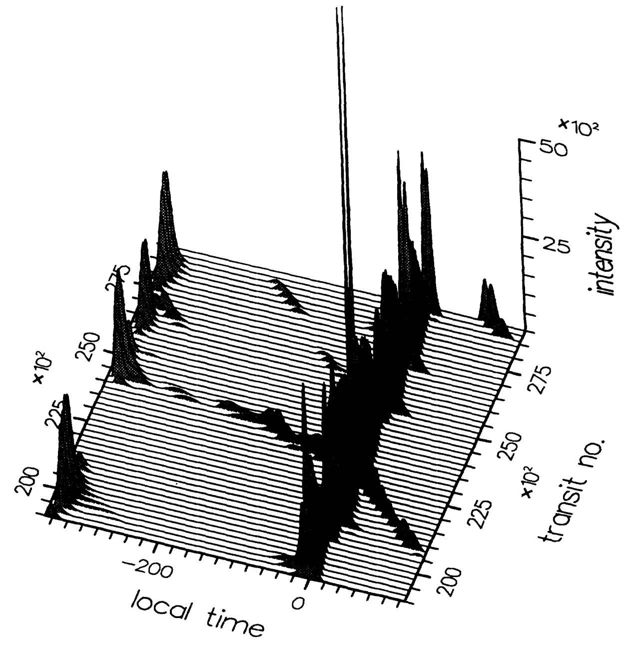

FIG. 19. Pulse profile evolutions displayed from 19 000 to 29 000 transits at 200 transit intervals for $t_m = -\Delta t$.

ing behavior becomes less distinct and the pulse form is less strongly restricted to the two preferred positions, as shown in Fig. 20 for $t_m = -4\Delta t$. In addition, the field no longer falls to spontaneous-emission noise level during any part of the cavity round-trip, indicating the complete collapse of mode locking.

In the above, we have concentrated on the effects of cavity mismatch because variation of this critical parameter, which must be possible in any experimental system, gives a wide range of dynamical responses. To complete our discussion, we briefly consider the lesser effects of pump-pulse amplitude and duration, and spontaneous-emission amplitude. For the first of these, we used the same parameters as above, set $t_m = 0$, and varied $A_{\max}$ from 0.1 to $1.0(A_{\max})_{\text{thr}}$. In each case, the behavior was qualitatively identical to that detailed above for $0.5(A_{\max})_{\text{thr}}$, resulting in slowly oscillating mode-locked pulses. The average parameters describing these pulses varied as follows: peak intensity $\propto A_{\max}^2$, pulse duration $\propto 1/A_{\max}$, and delay $\propto 1/A_{\max}$. A slight deviation from these laws was apparent for lower pump powers, probably due to the proximity of the mode-locking threshold. However, an exact determination of the threshold was not possible, because the pulse evolution slowed with decrease in pump power, taking in excess of 20 000 transits for $A_{\max} = 0.1(A_{\max})_{\text{thr}}$. This latter figure indicates an upper limit for the mode-locking threshold, which corresponds to a modulation depth of 10% of lasing threshold, and a cumulative pump rate 16 times above first lasing threshold, in reasonable agreement with experiment [2].

To consider the effects of pump-pulse duration, we returned to the original parameter values and varied t_{FWHM} from 70 to 140 ps, keeping the total pump energy (product $A_{\max} t_{\text{FWHM}}$) constant. The resulting pulse evolutions showed little variation. Although the ultimate oscillatory behavior became slightly more erratic with increase in t_{FWHM}, the average parameters describing these pulses varied by less than 10%. This weak dependence probably arises because for these examples in which $t_m = 0$ (see Fig. 4) the mode-locked pulse is remote from the pump pulse. A stronger dependence, such as that described in [5], would be expected if the mismatch was adjusted to bring the mode-locked pulse forward to directly interact with the gain modulation. Lastly, on the subject of pump-pulse shape, we note the almost negligible difference between pulse evolutions driven by Gaussian or $\text{sech}^2(t)$ pulses of the same energies.

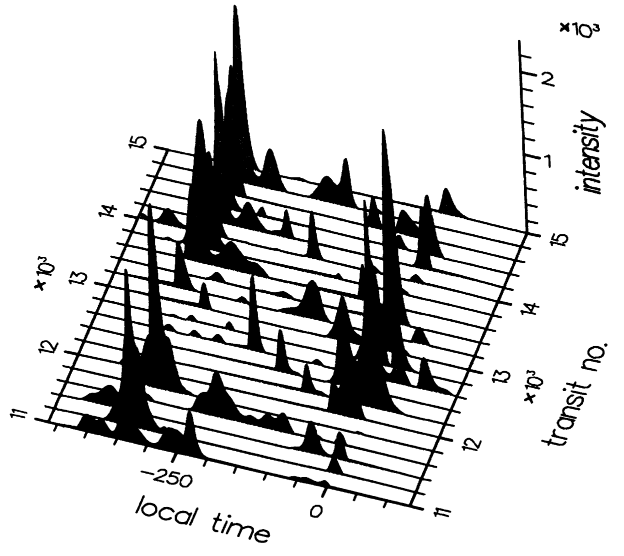

FIG. 20. Pulse profile evolutions displayed from 11 000 to 15 000 transits at 200 transit intervals for $t_m = -4\Delta t$.

Finally, we return briefly to the source of the large-scale fluctuations described in this paper, i.e., the spontaneous-emission noise, the emphasize their very weak dependence on the noise amplitude. Variation of A_s over four orders of magnitude from 10^{-4} to 10^{-8} showed pulse evolutions with final oscillations becoming slightly more erratic with increase in A_s, but with negligible variation in the average peak pulse powers and durations. A weak dependence was noted, however, in the pulse delay which increased from approximately 310 to 450 ps on decrease of A_s over this range.

IV. CONCLUSIONS

In this paper, we have presented a simple model based on traveling-wave equations to study the mode-locking dynamics of color-center lasers. Our computationally intensive approach differs from most others in its simulation of the mode-locking process using a one-dimensional partial differential equation, defined throughout the laser cavity. We have confirmed that fluctuations originating from spontaneous-emission noise, far out in the pulse wings, cause large-scale perturbations to the pulse profiles, and have established that these are indeed associated with *phase waves* [16] as suggested in [6]. However, unlike previous studies, we have shown that it is possible to minimize these perturbations by adjusting cavity mismatch, without destroying pulse quality, and thereby obtain an optimized, quasistationary, mode-locked pulse train. Such pulse trains were observed in a narrow window of mismatch values, within which their peak intensities and durations were seen to vary substantially. On further mismatch adjustment, the familiar asymmetric response characteristic of mode locking by synchronous pumping was obtained; however, to positive mismatch, the mode-locked pulses were established remote from the pump pulses, with a relatively slow decay in their quality, whereas to negative mismatch, a novel switching behavior, associated with the Fabry-Pérot geometry, was obtained.

ACKNOWLEDGMENTS

This work was carried out under the auspices of SERC Grant No. GR/F75070 and EEC twinning Grant No. SCI∗0325C. The computational facility used by the authors was provided by the SERC computational science initiative Grant No. GR/G13044.

APPENDIX A

To demonstrate the scaling of our equations, we begin with the two-level Maxwell-Bloch equations for a material subject to counterpropagating electric fields of the same carrier frequency (ω),

$$\begin{aligned}
&\pm\frac{c}{\eta}\frac{\partial\epsilon^{\pm}}{\partial z}+\frac{\partial\epsilon^{\pm}}{\partial t}=\frac{-i\omega N\mu}{\eta\epsilon}\rho_0^{\pm}\ ,\\
&\frac{\partial\rho_q^{+}}{\partial t}=-\gamma_2\rho_q^{+}+\frac{i\mu}{2\hbar}(\epsilon^{+}n_q+\epsilon^{-}n_{q+1})\quad(q\geq 0)\ ,\\
&\frac{\partial\rho_q^{-}}{\partial t}=-\gamma_2\rho_q^{-}+\frac{i\mu}{2\hbar}(\epsilon^{-}n_q^{*}+\epsilon^{+}n_{q+1}^{*})\quad(q\geq 0)\ ,\\
&\frac{\partial n_q}{\partial t}=-\gamma_1 n_q+\frac{i\mu}{\hbar}(\epsilon^{+*}\rho_q^{+}+\epsilon^{-*}\rho_{q-1}^{-}-\epsilon^{-}\rho_q^{-*}-\epsilon^{+}\rho_{q-1}^{-*})\quad(q>0)\ ,\\
&\frac{\partial n_0}{\partial t}=-\gamma_1(n_0-n_0^0)+\frac{i\mu}{\hbar}(\epsilon^{+*}\rho_0^{+}+\epsilon^{-*}\rho_0^{-}-\text{c.c.})\ .
\end{aligned}\tag{A1}$$

These equations are derived by the usual method of semiclassical laser theory, by coupling Maxwell's wave equation of the electric field with the two-level density matrix equations and requiring the resulting set to be self-consistent. Thus we have assumed plane-wave solutions of the form

$$\begin{aligned}
&E=\tfrac{1}{2}(\epsilon^{+}e^{i(\omega t-kz)}+\epsilon^{-}e^{i(\omega t+kz)}+\text{c.c.})\ ,\\
&P=N\mu\sum_{q=0}^{\infty}(\rho_q^{+}e^{i(\omega t-kz)}e^{-2iqkz}+\rho_q^{-}e^{i(\omega t+kz)}e^{+2iqkz}+\text{c.c.})\ ,\\
&n=n_0+\sum_{q=1}^{\infty}(n_q e^{-2iqkz}+\text{c.c})\ ,
\end{aligned}\tag{A2}$$

where $\epsilon^{\pm}$, $\rho^{\pm}$, and n are the slowly varying envelopes of the forward and backward fields, off-diagonal matrix elements, and difference in diagonal matrix elements $(n=\rho_{22}-\rho_{11})$. γ_1 $(1/t_1)$ and γ_2 $(1/t_2)$ are the phenomenological damping constants for n and ρ, which are taken to be equal for all Fourier components. N is the density of atoms and μ is the modulus of the transition dipole moment strength. η and ϵ are the material refractive index and permittivity. The term n_0^0 in the zeroth-order equation for n is a phenomenological pumping term.

There are, of course, many ways to scale these equations. Firstly, we write,

$$E^{\pm}=\frac{\mu\epsilon^{\pm}}{\hbar(\gamma_1\gamma_2)^{1/2}},\quad p_q^{\pm}=2i\left[\frac{\gamma_2}{\gamma_1}\right]^{1/2}\rho_q^{\pm},\quad n_q=n_q \tag{A3}$$

to give

$$\begin{aligned}
&\pm\frac{c}{\eta}\frac{\partial E^{\pm}}{\partial z}+\frac{\partial E^{\pm}}{\partial t}=-gp_0^{\pm}\ ,\\
&\frac{\partial p_q^{+}}{\partial t}=-\gamma_2(p_q^{+}+E^{+}n_q+E^{-}n_{q+1})\quad(q\geq 0)\ ,\\
&\frac{\partial p_q^{-}}{\partial t}=-\gamma_2(p_q^{-}+E^{-}n_q^{*}+E^{+}n_{q+1}^{*})\quad(q\geq 0)\ ,\\
&\frac{\partial n_q}{\partial t}=-\gamma_1[n_q-\tfrac{1}{2}(E^{+*}p_q^{+}+E^{-*}p_{q-1}^{-}+E^{-}p_q^{-*}+E^{+}p_{q-1}^{-*})]\quad(q>0)\ ,\\
&\frac{\partial n_0}{\partial t}=-\gamma_1[(n_0-n_0^0)-\tfrac{1}{2}(E^{+*}p_0^{+}+E^{-*}p_0^{-}+\text{c.c.})]\ ,
\end{aligned}\tag{A4}$$

where

$$g=\frac{\omega N\mu^2}{2\eta\epsilon\hbar\gamma_2} \tag{A5}$$

is the unsaturated gain constant per unit time. It is related to the cross section for stimulated emission (σ) by

$$g=\frac{c}{\eta}\frac{N\sigma}{2}\ . \tag{A6}$$

This scaled system is tidy because all terms of each of the material equations are multiplied by the same damping constant. However, we can do a little more. Following the standard approach when dealing with partial differential equations on a finite interval, we scale the longitudinal coordinate to the length of the laser medium (L) and the time to L divided by the phase velocity (c/η),

$$z'=\frac{z}{L},\quad t'=\frac{c}{\eta L}t\ . \tag{A7}$$

Introducing

$$\alpha_{L2}=\frac{\eta L}{c}g \tag{A8}$$

and

$$P_q^{\pm}=\alpha_{L2}p_q^{\pm},\quad D_q=\alpha_{L2}n_q,\quad A=D_0^0=\alpha_{L2}n_0^0\ , \tag{A9}$$

we further simplify the system by combining the gain and pump quantities to yield a single pump parameter. The following set of nonlinear, coupled partial differential equations is then in a form suitable for numerical solution and provides the basis for our investigations,

$$\begin{aligned}
&\pm\frac{\partial E^{\pm}}{\partial z'}+\frac{\partial E^{\pm}}{\partial t'}=-P_0^{\pm}\ ,\\
&\frac{\partial P_q^{+}}{\partial t'}=-\Gamma_2(P_q^{+}+E^{+}D_q+E^{-}D_{q+1})\quad (q\geq 0)\ ,\\
&\frac{\partial P_q^{-}}{\partial t'}=-\Gamma_2(P_q^{-}+E^{-}D_q^{*}+E^{+}D_{q+1}^{*})\quad (q\geq 0)\ ,\\
&\frac{\partial D_q}{\partial t'}=-\Gamma_1[D_q-\tfrac{1}{2}(E^{+*}P_q^{+}+E^{-*}P_{q-1}^{-}+E^{-}P_q^{-*}+E^{+}P_{q-1}^{-*})]\quad (q>0)\ ,\\
&\frac{\partial D_0}{\partial t'}=-\Gamma_1[(D_0-A)-\tfrac{1}{2}(E^{+*}P_0^{+}+E^{-*}P_0^{-}+\text{c.c.})]\ ,
\end{aligned} \tag{A10}$$

where

$$\Gamma_1=(\eta L/c)\gamma_1,\quad \Gamma_2=(\eta L/c)\gamma_2\ . \tag{A11}$$

To obtain Eqs. (1) we add the phenomenological source terms representing spontaneous emission $S^{\pm}$ to the right-hand sides of the equations for $P_0^{\pm}$, let $A\rightarrow A(t)$, and truncate this infinite system, retaining only terms for $q=0$ (higher level truncations can be similarly obtained).

The average power per unit area carried in the direction of propagation is given by the Poynting vector, which for the harmonic fields assumed above is

$$S_p^{+}=\tfrac{1}{2}\epsilon c|\epsilon^{+}|^2\quad (\text{W/m}^2)\ , \tag{A12}$$

for the positive traveling field. Applying the above scaling gives

$$S_p^{+}=\frac{\hbar\omega}{2\sigma t_1}|E^{+}|^2\quad (\text{W/m}^2)\ , \tag{A13}$$

in terms of the scaled electric field. Similarly, one can obtain the energy in a given pulse from

$$E_p=\frac{\hbar\omega}{2\sigma t_1}\frac{\eta L}{c}\int_{\text{pulse}}|E^{+}(z',t')|^2dt'\quad (\text{J/m}^2)\ . \tag{A14}$$

of which the fraction $(1-r_2^2)$ is output coupled.

APPENDIX B

Equations (1) are a pair of advective partial differential equations coupled through their source terms to a set of stochastic, ordinary differential equations. Thus the longitudinal variation of the medium variables is mediated only through the propagation of the forward- and backward-going electric fields. To numerically solve these equations we applied the second-order, finite difference scheme of Fleck [8] to obtain a system of five implicit difference equations. Examples of the two types of resulting equations, for E^{+} and P_0^{+}, are given by

$$E_j^{+n+1}-E_{j-1}^{+n}=-\frac{\Delta t'}{2}(P_{0j}^{+n+1}-P_{0j-1}^{+n})\ , \tag{B1}$$

and

$$\begin{aligned}
P_{0j}^{+n+1}=C_2P_{0j}^{+n}-\Gamma_2(A_2E_j^{+n}D_{0j}^{n}+B_2E_j^{+n+1}D_{0j}^{n+1})\\
+A_se^{i\phi_j^{+n+1}}\ ,
\end{aligned} \tag{B2}$$

where

$$\begin{aligned}
&C_2=e^{-\Gamma_2\Delta t'}\ ,\\
&A_2=\frac{1}{\Gamma_2}\left[\frac{1}{\Gamma_2\Delta t'}(1-e^{-\Gamma_2\Delta t'})-e^{-\Gamma_2\Delta t'}\right]\ ,\\
&B_2=\frac{1}{\Gamma_2}\left[1-\frac{1}{\Gamma_2\Delta t'}(1-e^{-\Gamma_2\Delta t'})\right]\ ,
\end{aligned} \tag{B3}$$

and n and j are the time and longitudinal grid point indices, respectively. The coefficients (C_1,A_1,B_1) for differencing the population difference equation are given by C_2, A_2, and B_2 with $\Gamma_2\rightarrow\Gamma_1$.

To solve the implicit difference equations we used either the explicit method suggested by Fleck [8] or a simple Newton iteration. In the former scheme, the forward extrapolated variables,

$$D_{0j}^{n+1}=2D_{0j}^{n}-D_{0j}^{n-1}\ , \tag{B4}$$

were substituted into the equations for the fields and polarizations, which were solved simultaneously for $E_j^{\pm n+1}$. The $E_j^{\pm n+1}$ were then substituted back into the original polarization and inversion equations (without forward extrapolation) to obtain $P_{0j}^{\pm n+1}$ and D_{0j}^{n+1}. In the latter scheme, the Newton iteration was performed on a system of equations of the form

$$\underline{\epsilon}_j^{n+1}=A^{-1}(\underline{v}_j^{n+1})[\underline{B}(\underline{u}_j^n,\underline{u}_{j-1}^n,\underline{u}_{j+1}^n)+\underline{C}(\underline{v}_j^{n+1})] , \quad \text{(B5)}$$

where $\underline{u}_j^n=(E_j^{+n},E_j^{-n},P_{0j}^{+n},P_{0j}^{+n},D_{0j}^n)$, $\underline{v}_j^n$ is the vector of iterated variables which converges to $\underline{u}_j^{n+1}$, A is a 5×5 matrix, and $\underline{B}$ and $\underline{C}$ are 5-vectors. Starting with a set of initial guesses for $\underline{v}_j^n$, this system is iterated until the deviations from the true solutions, $\underline{\epsilon}_j^{n+1}=\underline{u}_j^{n+1}-\underline{u}_j^n$, are sufficiently small. The random number generator used in each scheme was the routine RAN1 from Ref. [15].

A computation of 500 transit times for the discretization described above takes approximately 11 000 CPU seconds on an Intel *i*860 using the explicit scheme. The equivalent computation is between five and ten times as expensive using the implicit scheme, depending on the required accuracy. We note that for any given set of parameter values the computation time varies as $1/\Delta t^2$.

[1] G. H. C. New, Rep. Prog. Phys. **46**, 877 (1986).

[2] L. F. Mollenauer, in *Laser Handbook,* edited by M. L. Stitch and M. Bass (North-Holland, Amsterdam, 1985), Vol. 4, p. 208.

[3] Z. A. Yasa, Opt. Lett. **8**, 277 (1983).

[4] S. Kelly, G. H. C. New, and D. Wood, Appl. Phys. B **47**, 349 (1988).

[5] T. Kurobiro, K. Aoki, T. Segawa, and N. Takeuchi, Jpn. J. Appl. Phys. **29**, 1951 (1990).

[6] J. M. Catherall and G. H. C. New, IEEE J. Quantum Electron. **QE-22**, 1593 (1986).

[7] H. Avramopolous and G. H. C. New, Opt. Commun. **71**, 370 (1989).

[8] J. A. Fleck, Jr., Phys. Rev. B **1**, 84 (1970).

[9] L. F. Mollenhauer and R. H. Stolen, Opt. Lett. **9**, 13 (1984).

[10] J. Mark, L. Y. Lui, K. L. Hall, H. A. Haus, and E. P. Ippen, Opt. Lett. **14**, 48 (1989).

[11] E. M. Wright, W. J. Firth, and I. Galbraith, J. Opt. Soc. Am. B **2**, 383 (1985).

[12] G. D'Allesandro, A. Politi, and F. T. Arrechi, Europhys. Lett. **10**, 651 (1989).

[13] L. W. Casperson and M. F. H. Tarroja, J. Opt. Soc. Am. B **8**, 250 (1991).

[14] R. F. Fox, I. R. Gatland, R. Roy, and G. Vemuri, Phys. Rev. A **39**, 5938 (1988).

[15] W. H. Press, B. P. Flannery, S. A. Teukolsky, and W. T. Vetterling, *Numerical Recipes: The Art of Scientific Computing* (Cambridge University Press, Cambridge, England, 1986), p. 436.

[16] F. A. Hopf and E. A. Overman II, Phys. Rev. A **19**, 1180 (1979).

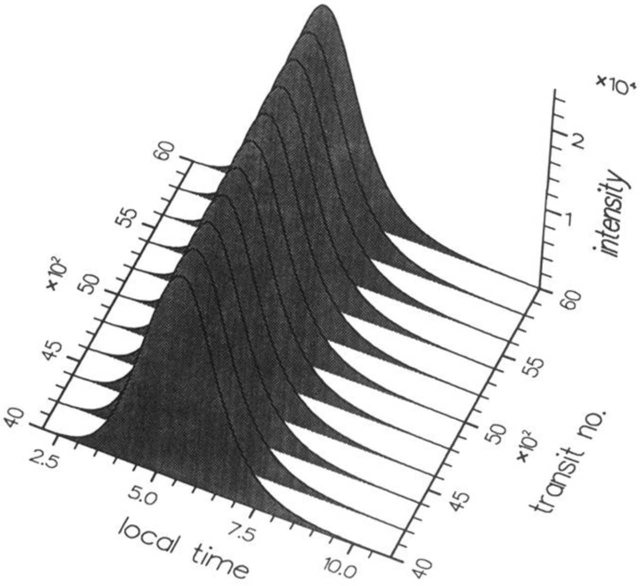

FIG. 10. Pulse profile evolutions displayed from 4000 to 6000 transits at 200 transit intervals for $t_m = -\Delta t/4$.

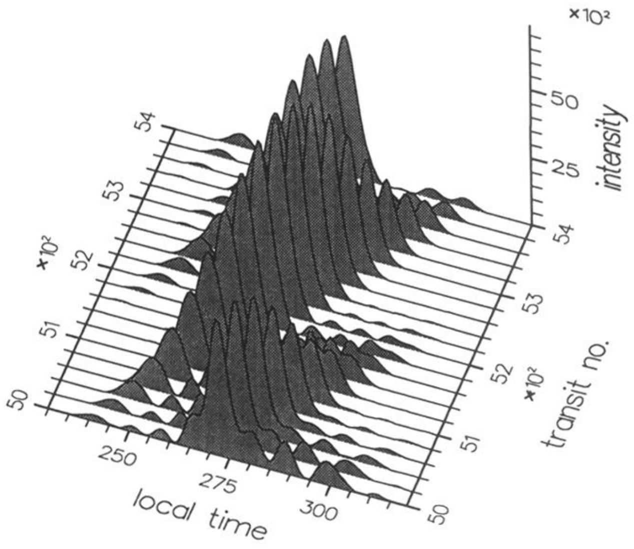

FIG. 16. Pulse profile evolutions displayed from 5000 to 5400 transits at 20 transit intervals for $t_m = 2\Delta t$.

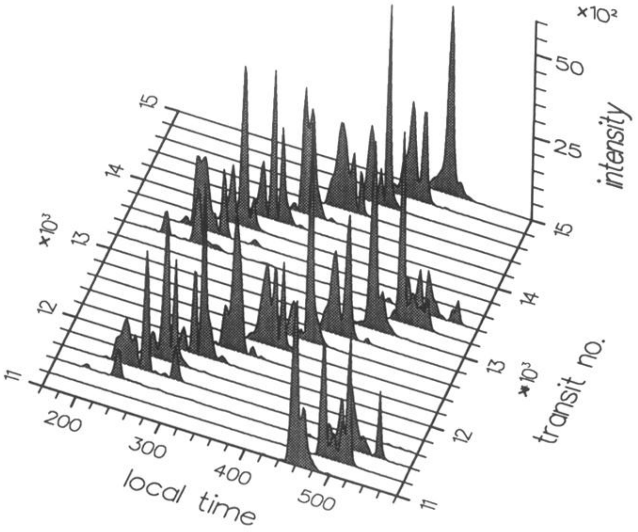

FIG. 18. Pulse profile evolutions displayed from 11 000 to 15 000 transits at 200 transit intervals for $t_m = 4\Delta t$.

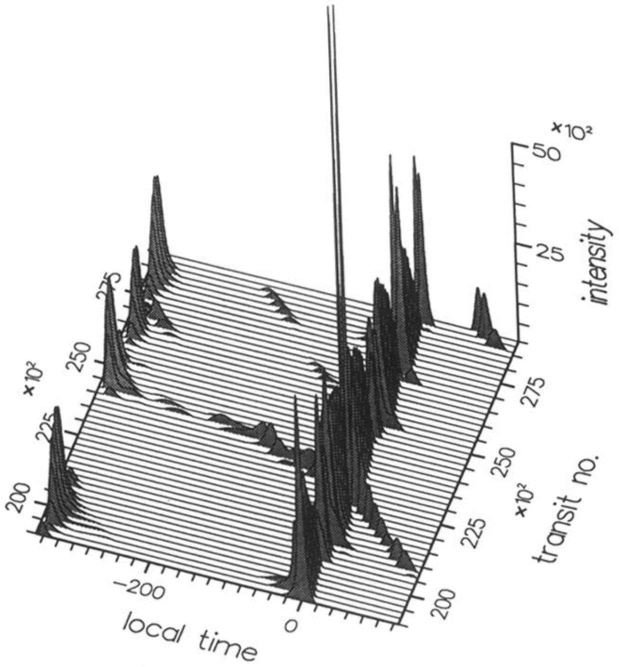

FIG. 19. Pulse profile evolutions displayed from 19 000 to 29 000 transits at 200 transit intervals for $t_m = -\Delta t$.

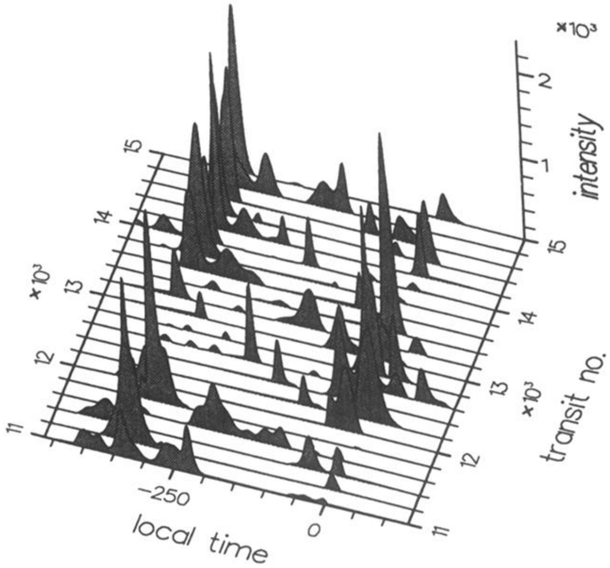

FIG. 20. Pulse profile evolutions displayed from 11 000 to 15 000 transits at 200 transit intervals for $t_m = -4\Delta t$.

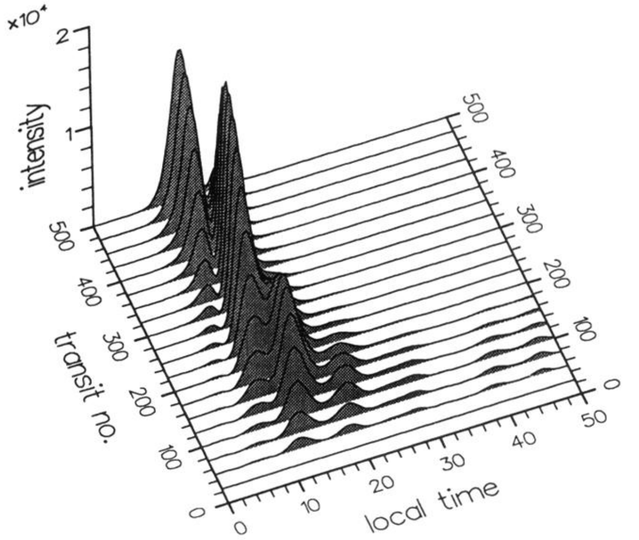

FIG. 3. Pulse profile evolutions $[|E^{+}(nz)^{2}|]$ over the first 500 transits displayed at 25 transit intervals. The pump pulse, which is centered at $t_{\text{loc}}=0$, is approximately 11 local time units wide (FWHM). Because $t_p=t_{\text{rt}}$ the pump-pulse transit number also corresponds to the cavity round-trip number, which is not true generally.

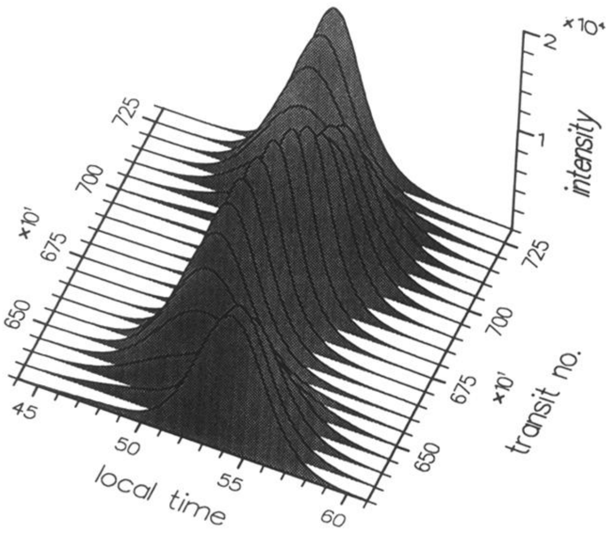

FIG. 7. Pulse profile evolutions in the final phase, displayed from 6300 to 7300 transits at 50 transit intervals.